

Electron-Magnon Interaction-Induced Topological Phase Transition in Magnetic Weyl Semimetals

Konstantinos Sourounis* and Aurélien Manchon†
Aix-Marseille Université, CNRS, CINaM, Marseille, France

Despite the tremendous interest raised by the recent realization of magnetic Weyl semimetals and the observation of giant anomalous Hall signals, most of the theories used to interpret experimental data overlook the magnetic fluctuations, which are ubiquitous in such materials and can massively impact topological and transport properties. In this work, we predict that in such magnetic topological systems, the interaction between electrons and magnons substantially destabilizes the Weyl nodes, leading to a topological phase transition below the Curie temperature. Remarkably, the sensitivity of the Weyl nodes to electron-magnon interaction depends on their spin chirality. We find that Weyl nodes with a trivial chirality are more sensitive to electron-magnon interactions than Weyl nodes presenting an inverted chirality, demonstrating the resilience of the latter compared to the former. Our results open perspectives for the interpretation of the transport signatures of Weyl semimetals, especially close to the Curie temperature.

Introduction - Magnetic topological materials, both insulators [1–3] and semimetals [4, 5], are currently under scrutiny as they can emulate high-energy physics such as the quantized magnetoelectric effect associated with axions [6–8] and the chiral anomaly associated with Weyl fermions [9, 10]. While the original realization of topological insulators was made by doping nonmagnetic topological insulators with magnetic impurities [11, 12], the identification and synthesis of intrinsic magnetic topological materials have made massive progress in the last few years [13–19]. With the realization of magnetic Weyl semimetals [5], there has been extensive theoretical work on their classification based on symmetries [20–22] and their anomalous transport properties [23–25]. One of the most intriguing hallmarks of these materials is the giant anomalous Hall effect associated with the Weyl nodes, detected in ferromagnetic topological semimetal candidates [26, 27] with cubic Heusler alloys taking the spotlight [28–32]. Whereas the topological transport properties of such systems have been studied thoroughly at the zero-temperature limit, the influence of magnetic fluctuations, ubiquitous at finite temperatures, has been largely overlooked.

Determining the topology of materials in the presence of interactions is a challenging topic as interactions break the well-defined nature of electronic quasiparticles [19, 33–37]. While the correct definition of topology in an interacting system is an open problem [38–40], the most widely used topological diagnosis is the N_3 -number [41–43], which converges towards the Chern number in the noninteracting limit. To date, most attention has been paid to materials whose topological properties are governed by electron correlations, such as topological Mott [44–47], Kondo [48, 49] or fractional insulators [50] and semimetals. One particularly interesting proposal is that

the electron-phonon interaction can induce a topological phase transition upon changing the temperature, as first proposed in Ref. [51, 52] and later confirmed by *ab initio* studies [53–56]. In this situation, the electron mass is enhanced by electron-phonon coupling, resulting in a temperature-dependent orbital gap, leading to the topological phase transition. In magnetic topological materials, where the topology is intimately related to the spin chirality of the wave function, the electron-magnon interaction is expected to induce interband transitions that can deteriorate the Berry curvature and, thereby, impact the topology. This interaction is crucial to properly understand the giant anomalous Hall signature recently reported in magnetic Weyl semimetals such as $\text{Co}_3\text{Sn}_2\text{S}_2$ [13–15, 18] or $(\text{Ni,Pt})\text{MnSb}$ [31].

In this Letter, we show how the electron-magnon interaction can control the topological phase of a magnetic topological semimetal and heavily impact its transport properties. Remarkably, we find that in a magnetic Weyl semimetal, this interaction enables temperature-

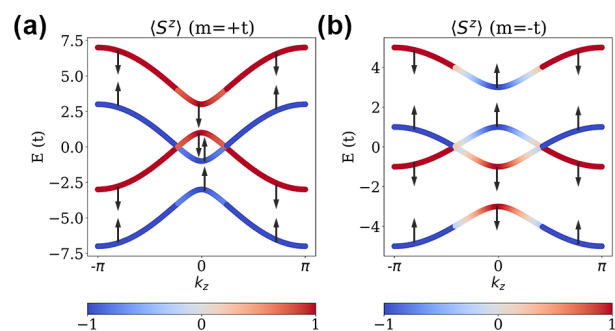


FIG. 1. The band structure of the magnetic Weyl semimetal projected on the spin chirality at $T = 0\text{K}$. The arrows indicate the direction of the energy shift induced by the electron-magnon self-energy, as explained in the main text. Two different regimes are considered: (a) the trivial ($m = +t$) and (b) the inverted ($m = -t$) one.

* konstantinos.sourounis@univ-amu.fr

† aurelien.manchon@univ-amu.fr

dependent topological phase transitions below the Curie temperature, and we demonstrate that the sensitivity of the Weyl nodes to the electron-magnon interaction depends on the chirality of the nodes.

Electron-Magnon Interaction - The magnetic Weyl semimetal is modeled by a four-band Hamiltonian with both spin ($\sigma = \uparrow, \downarrow$) and orbital ($\eta = A, B$) degrees of freedom, representing a magnetic cubic Heusler material as studied in Refs. [24, 51, 57]. The total Hamiltonian reads $\mathcal{H} = \mathcal{H}^e + \mathcal{H}^m + \mathcal{H}^{em}$, where \mathcal{H}^e and \mathcal{H}^m represent the electronic and magnetic systems, and \mathcal{H}^{em} their interaction. The electronic Hamiltonian reads

$$\mathcal{H}_{\mathbf{k}}^e = \mathbf{d}_{\mathbf{k}} \cdot \boldsymbol{\sigma} \otimes \tau^x + M_{\mathbf{k}} \sigma^0 \otimes \tau^z + \Delta \langle S^z \rangle \sigma^z \otimes \tau^0, \quad (1)$$

where τ^i and σ^i are Pauli matrices in the orbital and spin space respectively, τ^0, σ^0 are the identity matrices, $d_k^i = -2\lambda \sin k_i$ represent the spin-orbit coupling along the i -directions ($i = x, y, z$), and $M_{\mathbf{k}} = m + 2t(3 - \sum_i \cos k_i)$ is the mass parameter. Δ is the exchange between itinerant and localized electrons and $\langle S^z \rangle$ is the expectation value of the localized electron spins. In most theories, these spins are considered frozen, but magnetization quenching due to magnon-magnon interactions can easily be accounted for via a mean-field approach, e.g., $\langle S^z \rangle = S(1 - T/T_C)^{1/3}$, where the Curie temperature is $T_C = 8J$, J being the magnetic exchange. In the absence of magnetization ($\Delta = 0$), this Hamiltonian represents a Dirac semimetal. By tuning the magnetization, the system adopts two distinct phases, an insulating one (I), $\Delta < |m|$, and a Weyl semimetal phase (WSM), $\Delta > |m|$. In the I phase, the electronic bands are insulating in all directions, while in the WSM phase, two Weyl Points exist in the k_z direction as depicted in Fig. 1. In addition, switching the sign of m changes the spin chirality of Weyl nodes, as illustrated by the color scale in Fig. 1. In the following, we refer to $m > 0$ ($m < 0$) as the trivial (inverted) regime. When the chemical potential is set to zero, $\mu = 0$, this model is equivalent to a stack of 2D Chern Insulators along the k_z direction [58]. In this case, the anomalous Hall conductivity is proportional to the distance between the two Weyl points along this axis $\sigma_{xy} = (e^2/\pi h) \Delta_{WP}$, where Δ_{WP} is the distance in momentum space of the Weyl points, similar to its two-band version [4].

Let us now turn our attention to the magnetic system, described by

$$\mathcal{H}^m = -J \sum_{\langle ij \rangle} \mathbf{S}_i \cdot \mathbf{S}_j + K \sum_i (S_i^z)^2, \quad (2)$$

where J (>0) is the nearest-neighbor exchange interaction and K is the uniaxial anisotropy, taken perpendicular to the plane. In the presence of magnetic fluctuations, this Hamiltonian can be readily transformed in the magnon basis via Holstein-Primakoff transformation, as described in the Supplemental Materials [59]. Finally,

the interaction between the magnetic fluctuations and the itinerant electrons is given by

$$\mathcal{H}^{em} = \Delta \sqrt{\frac{S}{2}} \sum_i (S_i^+ \sigma_- + S_i^- \sigma_+) \otimes \tau^0. \quad (3)$$

Applying the Holstein-Primakoff transformation, the electron-magnon coupling can be rewritten in the second quantization representation

$$\mathcal{H}_{\mathbf{k}}^{em} = \Delta \sqrt{2S} \sum_{\mathbf{q}, \eta} \left(a_{\mathbf{q}} c_{\eta\downarrow, \mathbf{k}+\mathbf{q}}^\dagger c_{\eta\uparrow, \mathbf{k}} + a_{-\mathbf{q}}^\dagger c_{\uparrow\eta, \mathbf{k}+\mathbf{q}}^\dagger c_{\eta\downarrow, \mathbf{k}} \right). \quad (4)$$

Here $a_{\mathbf{q}}$ is the magnon annihilation operator, and $c_{\eta\sigma, \mathbf{k}}$ is the annihilation operation for an electron with orbital η and spin σ . Since the eigenstates of Eq. (1) are spin- and orbital-mixed, spin-flip processes induced by the electron-magnon scattering further mixes the bands thereby modifying their topology. To assess the impact of electron-magnon interaction on the band structure, we compute the electron self-energy using quantum field theory [60] and obtain

$$\begin{aligned} \hat{\Sigma}_{\mathbf{k}, \eta\downarrow, \eta'\downarrow}^{R/A}(\epsilon, T) &= \sum_{\mathbf{q}, \nu} \Phi_{\nu, \mathbf{k}+\mathbf{q}}^{\eta\downarrow, \eta'\downarrow} \frac{n_F(\epsilon_{\nu, \mathbf{k}+\mathbf{q}}) + n_B(\omega_{\mathbf{q}})}{\epsilon \pm i0^+ - \epsilon_{\nu, \mathbf{k}+\mathbf{q}} + \omega_{\mathbf{q}}}, \quad (5) \\ \hat{\Sigma}_{\mathbf{k}, \eta\uparrow, \eta'\uparrow}^{R/A}(\epsilon, T) &= \sum_{\mathbf{q}, \nu} \Phi_{\nu, \mathbf{k}+\mathbf{q}}^{\eta\uparrow, \eta'\uparrow} \frac{1 - n_F(\epsilon_{\nu, \mathbf{k}+\mathbf{q}}) + n_B(\omega_{\mathbf{q}})}{\epsilon \pm i0^+ - \epsilon_{\nu, \mathbf{k}+\mathbf{q}} - \omega_{\mathbf{q}}}, \quad (6) \end{aligned}$$

where n_F (n_B) is the Fermi-Dirac (Bose-Einstein) distribution of the electrons (magnons). The matrix elements $\Phi_{\nu, \mathbf{k}}^{\eta\sigma, \eta'\sigma'}$ and the calculation of self-energies are given explicitly in the Supplementary Material [61]. For the temperature range that we consider, only the distribution of the magnons is affected and the distribution of electrons can be approximated by a step function. The numerical broadening 0^+ is set to $0.1t$.

The electron-magnon interaction in a ferromagnetic metal causes the emission (absorption) of a magnon and the annihilation (creation) of an electron with spin down (up). This interaction causes a softening of the spin splitting of the ferromagnet, which, in the absence of spin-orbit coupling, can be written for each sublattice η as, $\Delta_{eff}^\eta = 2\Delta + \Sigma_{\eta, \downarrow} - \Sigma_{\eta, \uparrow}$ [62]. In the trivial case, $m = +t$, electrons in the ferromagnetic Weyl model have a similar spin polarization as a ferromagnetic metal, as depicted in Fig. 1 (a). As such, it is expected to accelerate the softening of the magnetization, $\langle S^z \rangle(T)$, together with the magnon-magnon interaction mentioned above. In the inverted regime, $m = -t$, the spin chirality is reversed, as depicted in Fig. 1 (b), which causes the increase of the effective magnetization Δ_{eff} in the region between the Weyl points, in competition with the effective softening. Overall, the effect is balanced, and the Weyl points survive at higher temperatures than in the trivial regime.

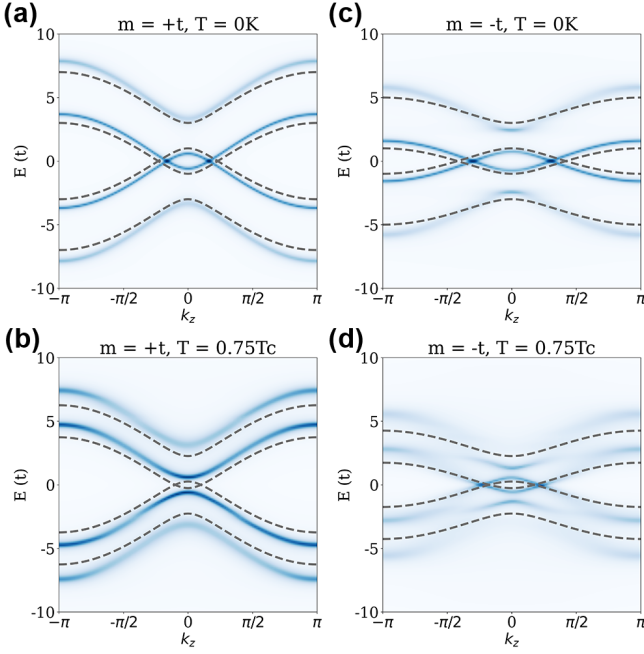


FIG. 2. The spectral function of the electrons (color) given by Eq. (7) versus the non-interacting spectrum (dashed lines) for (a) $m = +t$, $T = 0\text{K}$, (b) $m = +t$, $T = 0.75T_c$, (c) $m = -t$, $T = 0\text{K}$, (d) $m = -t$, $T = 0.75T_c$. The other parameters are set to $t = 1$, $\Delta = 2t$, $\lambda = t$, $S = 1$, $J = t/100$, $K = J/10$.

We first evaluate the ability of the interaction to impact the electrons' spectrum at zero and finite temperatures. To do so, we calculate the one-electron spectral function

$$A_{\mathbf{k}}(\epsilon) = -\frac{1}{\pi} \text{Im}(\text{Tr}[G_{\mathbf{k}}^R(\epsilon)]), \quad (7)$$

where the Green's function is in the Bloch basis, as discussed in [61], $G_{\mathbf{k}}^{R/A}(\epsilon) = (\epsilon \pm i\Gamma - \mathcal{H}_{\mathbf{k}}^e - \Sigma_{\mathbf{k}}^{R/A}(\epsilon, T))^{-1}$, where Γ is a homogeneous broadening due, e.g., to impurity scattering. Figure 2 displays the interacting spectral function (color) compared to the non-interacting spectrum of the electrons (grey dashed lines). Throughout this work, we adopt the set of parameters: $t = 1$, $\Delta = 2t$, $\lambda = t$, $S = 1$, $J = t/100$, $K = J/10$ and two different cases $m = \pm t$ [61]. For $T = 0\text{K}$ [Fig. 2(a,c)], the only contribution of the electron-magnon interaction is the zero-point fluctuation, and at $T = 0.75T_c$ [Fig. 2(b,d)], the thermally excited magnons greatly enhance the interaction. We can see in Fig. 2(a) and (c) that for both $m = \pm t$ cases, the interactions bring the Weyl points closer to each other compared to the non-interacting case, which indicates a weaker topology and a reduced anomalous Hall transport. However, at higher temperatures [Fig. 2(b,d)], once the thermal magnons take over, the two cases diverge. For $m = +t$, the Weyl points are annihilated by the interactions, *before* the Curie temperature is reached. This result demonstrates that the topology is

highly sensitive to temperature, and the geometrical contribution to the Hall transport is expected to vanish. For $m = -t$, the location of the Weyl points is only slightly affected by the temperature, indicating that the topological features may remain resilient even at high temperatures. Nevertheless, the bands are strongly broadened due to interactions, which can potentially impact transport by increasing diffusion.

Interacting Topology and Transport - To assess how these interactions affect the topology and Hall transport of the magnetic Weyl semimetal, we first compute the two-dimensional many-body topological number [41, 44]

$$N_3(k_z) = \frac{e^2}{h} \int d\eta \int dk_x dk_y \times \text{Tr}[G_{\mathbf{k}}^T(\partial_{\eta} G_{\mathbf{k}}^{-1}) G_{\mathbf{k}}^T(\partial_{k_x} G_{\mathbf{k}}^{-1}) G_{\mathbf{k}}^T(\partial_{k_y} G_{\mathbf{k}}^{-1}) - (x \leftrightarrow y)], \quad (8)$$

which is resolved in the k_z direction and where $\hat{G}_{\mathbf{k}}^T(\eta) = (i\eta - \mathcal{H}_{\mathbf{k}}^e - \Sigma_{\mathbf{k}}^T(\eta, T))^{-1}$ is the topological Green's function. To convert the retarded Green's functions and self-energies into the topological ones, we make the substitution $\epsilon + i\Gamma \rightarrow i\eta$, where the integration in Eq. (8) is over η . The advantage of this expression is that it accounts for changes in the spectrum, geometry, and broadening of the quasiparticles. This number is equivalent to the non-interacting Chern number in two dimensions, and it allows us to evaluate the topology at each k_z point.

In addition, to further confirm the topological nature of the interacting picture, we compute the intrinsic contribution to the anomalous Hall conductivity via Green's function method [63]

$$\sigma_{xy}(k_z) = \frac{e^2}{h} \int d\epsilon n_F(\epsilon) \int dk_x dk_y \times \text{Tr} \{ \partial_{k_x} G_{\mathbf{k}}^{-1} (G_{\mathbf{k}}^R - G_{\mathbf{k}}^A) \partial_{k_y} G_{\mathbf{k}}^{-1} (\partial_{\epsilon} G_{\mathbf{k}}^R + \partial_{\epsilon} G_{\mathbf{k}}^A) - (x \leftrightarrow y) \} \quad (9)$$

where $\partial_{k_i} G_{\mathbf{k}}^{-1} = -(\partial_{k_i} \mathcal{H}_{\mathbf{k}}^e + \partial_{k_i} \Sigma_{\mathbf{k}}^R(\eta, T))$ and $\partial_{\epsilon} G_{\mathbf{k}}^{R/A} = -(G_{\mathbf{k}}^{R/A}) \cdot (1 - \partial_{\epsilon} \Sigma_{\mathbf{k}}^{R/A}(\epsilon, T)) \cdot (G_{\mathbf{k}}^{R/A})$. For simplicity, we have considered $\partial_{\epsilon/\eta} \Sigma_{\mathbf{k}}(\epsilon, T) \approx 0$. Equation (9) is the Fermi sea contribution to the transport, equivalent to the anomalous Hall conductivity due to Berry curvature in the non-interacting limit.

For the magnetic Weyl semimetal model we employ, it is known that the Hall conductivity in the z -direction is proportional to the distance between the Weyl points, the length of the Fermi arc [4], of the system, which gives a direct connection between conductivity and topology. In Fig. 3, we calculate the many-body topological number N_3 using Eq. (8) (red symbols) and the anomalous Hall conductivity σ_{xy} using Eq. (9) (blue symbols), for the same configurations as in Fig. 2.

In the absence of interactions (superscripts (0), dashed lines), the values of both N_3 and σ_{xy} tend to be quantized to 1 for k_z inside the topological region (i.e., at

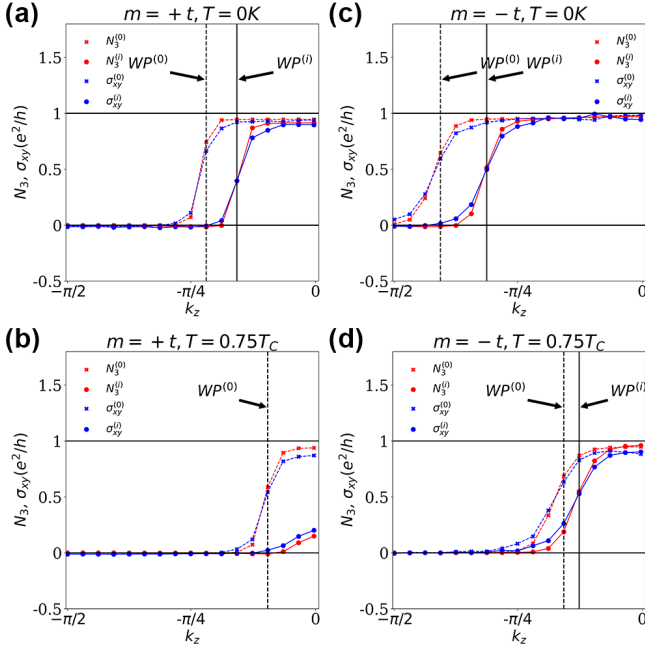


FIG. 3. The non-interacting and interacting many-body topological number, $N_3^{(0)}$ and $N_3^{(i)}$ [see Eq. (8)], and the corresponding anomalous Hall conductivity, $\sigma_{xy}^{(0)}$ and $\sigma_{xy}^{(i)}$ [see Eq. (9)], for the same configuration as in Fig. 2: (a) $m = +t$, $T = 0K$ (b) $m = +t$, $T = 0.75T_c$ (c) $m = -t$, $T = 0K$ (d) $m = -t$, $T = 0.75T_c$. The Weyl points, $WP^{(0,i)}$, are indicated by the vertical lines. We set $\Gamma = 0.2t$ in Eq. (9).

the right-hand side of $WP^{(0)}$ and zero outside it (at the left-hand side of $WP^{(0)}$). In the presence of interactions, the many-body calculations confirm the observations from the spectral properties in Fig. 2. In Fig. 3(a) and (c), in both regimes ($m = \pm t$) the distances of the Weyl points (solid vertical lines) are closer than the non-interacting calculation (dashed vertical lines). When the temperature increases, the results of the two regimes differ. For $m = +t$ [Fig. 3(b)], we see that interactions destroy the topology at high temperatures, and both N_3 and σ_{xy} vanish in this limit. For $m = -t$ [Fig. 3(d)], both topological and transport properties survive even at high temperatures.

In Fig. 4, we plot the phase diagram of the anomalous Hall conductivity [Eq. (9)] as a function of the temperature and the mass term m , with and without interactions. We compute the ratio between the conductivity at temperature T and the conductivity at zero temperature. In Fig. 4(a), we consider only the influence of the magnetization quenching due to magnon-magnon interaction, $\sigma_{xy}^{(0)}(T)/\sigma_{xy}^{(0)}(T = 0K)$, whereas in Fig. 4(b), we include the influence of the electron-magnon interaction, $\sigma_{xy}^{(i)}(T)/\sigma_{xy}^{(0)}(T = 0K)$. In the absence of interactions [Fig. 4 (a)], the trivial ($m > 0$) and inverted regimes ($m < 0$) exhibit a similar temperature dependence. Close to $m = 0$, the conductivity vanishes at

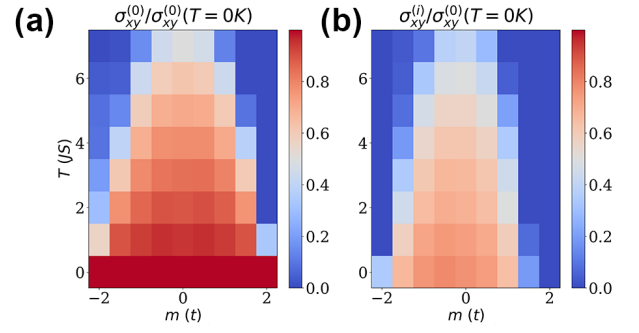


FIG. 4. The phase diagram of the anomalous Hall conductivity as a function of temperature from Eq. (9) of the (a) non-interacting (0) and (b) the interacting system (i) for different values of the mass of orbitals m . The magnetization quenching due to magnon-magnon interaction is accounted for in both cases $\langle S^z \rangle$.

the Curie temperature as the system goes from a ferromagnetic to a paramagnetic state. Away from $m = 0$, the conductivity vanishes at lower temperatures as the system transits toward the insulating phase. In the presence of interactions [Fig. 4 (b)], the picture is different. First, at zero temperature, the conductivity is substantially reduced compared to the noninteracting case due to the onset of zero-point magnetic fluctuations. Furthermore, the phase diagram is more asymmetric. In the trivial regime ($m > 0$), the electron-magnon interaction cooperates with the magnon softening, causing a decrease of the conductivity at lower temperatures than in the noninteracting case [Fig. 4 (a)]. In the inverted regime ($m < 0$), the two effects compete, as discussed above, and the conductivity survives at higher temperatures. Thus, the presence of the inverted spin chirality enforces the resilience of the topological state.

Conclusions - Our model demonstrates that electron-magnon interactions can massively impact the topology and the associated anomalous Hall transport in magnetic Weyl semimetals. Remarkably, we find that depending on the spin chirality in the vicinity of the Weyl nodes, the electron-magnon interaction either competes or cooperates with the magnon-magnon interaction, suggesting that the inverted spin chirality is more resilient against thermal fluctuations than the trivial case. This prediction sheds light on the recent experiments performed on $\text{Co}_3\text{Sn}_2\text{S}_2$ [13, 15, 18], $\text{Co}_2\text{Mn}(\text{Ga}, \text{Al})$ [14, 28] or $(\text{Ni}, \text{Pt})\text{MnSb}$ [31]. In these materials, the anomalous Hall effect is attributed to the joint contribution of the Weyl points, possibly nodal rings, but also the Berry curvature of the other bands crossing the Fermi level. Since the impact of the electron-magnon interaction depends on the spin chirality, one can reasonably expect that different spots in the band structure may behave differently upon increasing the temperature.

An important open question is the competing role of

electron-phonon interactions. Indeed, while both mechanisms transfer momentum between the electron and the bosonic bath, the electron-magnon interaction induces spin-flip, directly affecting the chirality of the eigenstates. As a result, the interplay between electron-phonon, electron-magnon, and magnon-magnon interactions results in an intricate temperature dependence of the topology. Whereas the electron-magnon and magnon-magnon interactions are controlled by the Curie temperature (ranging from 176 to 660 K in recently synthesized Weyl semimetals), the electron-phonon interactions are rather governed by Debye temperature (typically, 300-400 K in most metals). Consequently, we expect electron-magnon interactions to dominate over electron-phonon interaction in low Curie temperature Weyl semimetals, such as $\text{Co}_3\text{Sn}_2\text{S}_2$ ($T_C=176$ K), whereas in $(\text{Ni,Pt})\text{MnSb}$ ($T_C=560-660$ K), both effects should affect the topology. To address this issue, an exciting possible development would be computing the geometric properties of electron-magnon interaction via *ab initio* methods, similar to the extensively studied electron-phonon interaction [64].

K. S. thanks Diego García Ovalle and Armando Pezo for fruitful discussions. K.S. and A.M. acknowledge support from the Excellence Initiative of Aix-Marseille Université–A*Midex, a French Investissements d’Avenir” program.

-
- [1] M. Z. Hasan and C. L. Kane, Colloquium: Topological insulators, *Rev. Mod. Phys.* **82**, 3045 (2010).
- [2] X.-L. Qi and S.-C. Zhang, Topological insulators and superconductors, *Rev. Mod. Phys.* **83**, 1057 (2011).
- [3] Y. Tokura, K. Yasuda, and A. Tsukazaki, Magnetic topological insulators, *Nature Reviews Physics* **1**, 126 (2019).
- [4] N. P. Armitage, E. J. Mele, and A. Vishwanath, Weyl and dirac semimetals in three-dimensional solids, *Rev. Mod. Phys.* **90**, 015001 (2018).
- [5] B. A. Bernevig, C. Felser, and H. Beidenkopf, Progress and prospects in magnetic topological materials, *Nature* **603**, 41 (2022).
- [6] X.-L. Qi, T. L. Hughes, and S.-C. Zhang, Topological field theory of time-reversal invariant insulators, *Phys. Rev. B* **78**, 195424 (2008).
- [7] A. M. Essin, J. E. Moore, and D. Vanderbilt, Magneto-electric polarizability and axion electrodynamics in crystalline insulators, *Phys. Rev. Lett.* **102**, 146805 (2009).
- [8] C. Liu, Y. Wang, H. Li, Y. Wu, Y. Li, J. Li, K. He, Y. Xu, J. Zhang, and Y. Wang, Robust axion insulator and chern insulator phases in a two-dimensional antiferromagnetic topological insulator, *Nature Materials* **19**, 522 (2020).
- [9] A. A. Zyuzin and A. A. Burkov, Topological response in weyl semimetals and the chiral anomaly, *Phys. Rev. B* **86**, 115133 (2012).
- [10] D. T. Son and B. Z. Spivak, Chiral anomaly and classical negative magnetoresistance of weyl metals, *Phys. Rev. B* **88**, 104412 (2013).
- [11] C.-Z. Chang, J. Zhang, X. Feng, J. Shen, Z. Zhang, M. Guo, K. Li, Y. Ou, P. Wei, L.-L. Wang, Z.-Q. Ji, Y. Feng, S. Ji, X. Chen, J. Jia, X. Dai, Z. Fang, S.-C. Zhang, K. He, Y. Wang, L. Lu, X.-C. Ma, and Q.-K. Xue, Experimental observation of the quantum anomalous hall effect in a magnetic topological insulator, *Science* **340**, 167 (2013).
- [12] C.-Z. Chang, W. Zhao, D. Y. Kim, H. Zhang, B. A. As-saf, D. Heiman, S.-C. Zhang, C. Liu, M. H. W. Chan, and J. S. Moodera, High-precision realization of robust quantum anomalous hall state in a hard ferromagnetic topological insulator, *Nature Materials* **14**, 473 (2015).
- [13] N. Morali, R. Batabyal, P. K. Nag, E. Liu, Q. Xu, Y. Sun, B. Yan, C. Felser, N. Avraham, and H. Beidenkopf, Fermi-arc diversity on surface terminations of the magnetic weyl semimetal $\text{co}_3\text{sn}_2\text{s}_2$, *Science* **365**, 1286 (2019).
- [14] I. Belopolski, K. Manna, D. S. Sanchez, G. Chang, B. Ernst, J. Yin, S. S. Zhang, T. Cochran, N. Shumiya, H. Zheng, B. Singh, G. Bian, D. Multer, M. Litskevich, X. Zhou, S.-M. Huang, B. Wang, T.-R. Chang, S.-Y. Xu, A. Bansil, C. Felser, H. Lin, and M. Z. Hasan, Discovery of topological weyl fermion lines and drumhead surface states in a room temperature magnet, *Science* **365**, 1278 (2019).
- [15] D. F. Liu, A. J. Liang, E. K. Liu, Q. N. Xu, Y. W. Li, C. Chen, D. Pei, W. J. Shi, S. K. Mo, P. Dudin, T. Kim, C. Cacho, G. Li, Y. Sun, L. X. Yang, Z. K. Liu, S. S. P. Parkin, C. Felser, and Y. L. Chen, Magnetic weyl semimetal phase in a kagomé crystal, *Science* **365**, 1282 (2019).
- [16] M. M. Otrokov, I. I. Klimovskikh, H. Bentmann, D. Estyunin, A. Zeugner, Z. S. Aliev, S. Gaß, A. U. B. Wolter, A. V. Koroleva, A. M. Shikin, M. Blanco-Rey, M. Hoffmann, I. P. Rusinov, A. Y. Vyazovskaya, S. V. Ere-meev, Y. M. Koroteev, V. M. Kuznetsov, F. Freyre, J. Sánchez-Barriga, I. R. Amiraslanov, M. B. Babanly, N. T. Mamedov, N. A. Abdullayev, V. N. Zverev, A. Alfonsov, V. Kataev, B. Büchner, E. F. Schwier, S. Kumar, A. Kimura, L. Petaccia, G. Di Santo, R. C. Vidal, S. Schatz, K. Kißner, M. Ünzelmann, C. H. Min, S. Moser, T. R. F. Peixoto, F. Reinert, A. Ernst, P. M. Echenique, A. Isaeva, and E. V. Chulkov, Prediction and observation of an antiferromagnetic topological insulator, *Nature* **576**, 416 (2019).
- [17] Y. Deng, Y. Yu, M. Z. Shi, Z. Guo, Z. Xu, J. Wang, X. H. Chen, and Y. Zhang, Quantum anomalous hall effect in intrinsic magnetic topological insulator $\text{mnbij}_2\text{te}_3$, *Science* **367**, 895 (2020).
- [18] Electronic correlations and flattened band in magnetic weyl semimetal candidate $\text{co}_3\text{sn}_2\text{s}_2$, *Nature Communications* **11**, 3985 (2020).
- [19] I. Belopolski, T. A. Cochran, X. Liu, Z.-J. Cheng, X. P. Yang, Z. Guguchia, S. S. Tsirkin, J.-X. Yin, P. Vir, G. S. Thakur, S. S. Zhang, J. Zhang, K. Kaznatcheev, G. Cheng, G. Chang, D. Multer, N. Shumiya, M. Litskevich, E. Vescovo, T. K. Kim, C. Cacho, N. Yao, C. Felser, T. Neupert, and M. Z. Hasan, Signatures of weyl fermion annihilation in a correlated kagome magnet, *Phys. Rev. Lett.* **127**, 256403 (2021).
- [20] Y. Xu, L. Elcoro, Z.-D. Song, B. J. Wieder, M. G. Vergniory, N. Regnault, Y. Chen, C. Felser, and B. A. Bernevig, High-throughput calculations of magnetic topological materials, *Nature* **586**, 702 (2020).
- [21] L. Elcoro, B. J. Wieder, Z. Song, Y. Xu, B. Bradlyn, and B. A. Bernevig, Magnetic topological quantum chemistry,

- Nature Communications* **12**, 5965 (2021).
- [22] I. Robredo, Y. Xu, Y. Jiang, C. Felser, B. A. Bernevig, L. Elcoro, N. Regnault, and M. G. Vergniory, New magnetic topological materials from high-throughput search, arXiv preprint arXiv:2408.16851 (2024).
- [23] K. Manna, L. Muechler, T.-H. Kao, R. Stinchhoff, Y. Zhang, J. Gooth, N. Kumar, G. Kreiner, K. Koepf, R. Car, J. Kübler, G. H. Fecher, C. Shekhar, Y. Sun, and C. Felser, From colossal to zero: Controlling the anomalous hall effect in magnetic heusler compounds via berry curvature design, *Phys. Rev. X* **8**, 041045 (2018).
- [24] J. Noky, Y. Zhang, J. Gooth, C. Felser, and Y. Sun, Giant anomalous hall and nernst effect in magnetic cubic heusler compounds, *npj Computational Materials* **6**, 77 (2020).
- [25] K. Samanta, J. Noky, I. Robredo, J. Kuebler, M. G. Vergniory, and C. Felser, Large anomalous hall, nernst effect and topological phases in the 3d-4d/5d-based oxide double perovskites, *npj Computational Materials* **9**, 167 (2023).
- [26] E. Liu, Y. Sun, N. Kumar, L. Muechler, A. Sun, L. Jiao, S.-Y. Yang, D. Liu, A. Liang, Q. Xu, J. Kroder, V. Süß, H. Borrmann, C. Shekhar, Z. Wang, C. Xi, W. Wang, W. Schnelle, S. Wirth, Y. Chen, S. T. B. Goennenwein, and C. Felser, Giant anomalous hall effect in a ferromagnetic kagome-lattice semimetal, *Nature Physics* **14**, 1125 (2018).
- [27] K. Kim, J. Seo, E. Lee, K.-T. Ko, B. S. Kim, B. G. Jang, J. M. Ok, J. Lee, Y. J. Jo, W. Kang, J. H. Shim, C. Kim, H. W. Yeom, B. I. Min, B.-J. Yang, and J. S. Kim, Large anomalous hall current induced by topological nodal lines in a ferromagnetic van der waals semimetal, *Nature Materials* **17**, 794 (2018).
- [28] P. Li, J. Koo, W. Ning, J. Li, L. Miao, L. Min, Y. Zhu, Y. Wang, N. Alem, C.-X. Liu, Z. Mao, and B. Yan, Giant room temperature anomalous hall effect and tunable topology in a ferromagnetic topological semimetal Co_2MnAl , *Nature Communications* **11**, 3476 (2020).
- [29] S. Singh, J. Noky, S. Bhattacharya, P. Vir, Y. Sun, N. Kumar, C. Felser, and C. Shekhar, Anisotropic nodal-line-derived large anomalous hall conductivity in ZrMn_2P and HfMn_2P , *Advanced Materials* **33**, 2104126 (2021).
- [30] S. N. Guin, Q. Xu, N. Kumar, H.-H. Kung, S. Dufresne, C. Le, P. Vir, M. Michiardi, T. Pedersen, S. Gorovikov, S. Zhdanovich, K. Manna, G. Auffermann, W. Schnelle, J. Gooth, C. Shekhar, A. Damascelli, Y. Sun, and C. Felser, 2d-berry-curvature-driven large anomalous hall effect in layered topological nodal-line material, *Advanced Materials* **33**, 2006301 (2021).
- [31] S. Singh, A. García-Page, J. Noky, S. Roychowdhury, M. G. Vergniory, H. Borrmann, H.-H. Klauss, C. Felser, and C. Shekhar, Extended berry curvature tail in ferromagnetic weyl semimetals NiMn_2Sb and PtMn_2Sb , *Advanced Science* **11**, 2404495 (2024).
- [32] S. Chatterjee, J. Sau, S. Samanta, B. Ghosh, N. Kumar, M. Kumar, and K. Mandal, Nodal-line and triple point fermion induced anomalous hall effect in the topological heusler compound Co_2CrGa , *Phys. Rev. B* **107**, 125138 (2023).
- [33] X. Wan, A. M. Turner, A. Vishwanath, and S. Y. Savrasov, Topological semimetal and fermi-arc surface states in the electronic structure of pyrochlore iridates, *Phys. Rev. B* **83**, 205101 (2011).
- [34] W. Witczak-Krempa and Y. B. Kim, Topological and magnetic phases of interacting electrons in the pyrochlore iridates, *Phys. Rev. B* **85**, 045124 (2012).
- [35] K. Kuroda, T. Tomita, M.-T. Suzuki, C. Bareille, A. A. Nugroho, P. Goswami, M. Ochi, M. Ikhlas, M. Nakayama, S. Akebi, R. Noguchi, R. Ishii, N. Inami, K. Ono, H. Kumigashira, A. Varykhalov, T. Muro, T. Koretsune, R. Arita, S. Shin, T. Kondo, and S. Nakatsuji, Evidence for magnetic weyl fermions in a correlated metal, *Nature Materials* **16**, 1090 (2017).
- [36] J.-X. Yin, S. S. Zhang, H. Li, K. Jiang, G. Chang, B. Zhang, B. Lian, C. Xiang, I. Belopolski, H. Zheng, T. A. Cochran, S.-Y. Xu, G. Bian, K. Liu, T.-R. Chang, H. Lin, Z.-Y. Lu, Z. Wang, S. Jia, W. Wang, and M. Z. Hasan, Giant and anisotropic many-body spin-orbit tunability in a strongly correlated kagome magnet, *Nature* **562**, 91 (2018).
- [37] M. O. Soldini, N. Astrakhantsev, M. Iraola, A. Tiwari, M. H. Fischer, R. Valentí, M. G. Vergniory, G. Wagner, and T. Neupert, Interacting topological quantum chemistry of mott atomic limits, *Phys. Rev. B* **107**, 245145 (2023).
- [38] J. Zhao, P. Mai, B. Bradlyn, and P. Phillips, Failure of topological invariants in strongly correlated matter, *Phys. Rev. Lett.* **131**, 106601 (2023).
- [39] L. Peralta Gavensky, S. Sachdev, and N. Goldman, Connecting the many-body chern number to luttinger's theorem through středa's formula, *Phys. Rev. Lett.* **131**, 236601 (2023).
- [40] C. Setty, F. Xie, S. Sur, L. Chen, M. G. Vergniory, and Q. Si, Electronic properties, correlated topology, and green's function zeros, *Phys. Rev. Res.* **6**, 033235 (2024).
- [41] Z. Wang and S.-C. Zhang, Simplified topological invariants for interacting insulators, *Phys. Rev. X* **2**, 031008 (2012).
- [42] V. Gurarie, Single-particle green's functions and interacting topological insulators, *Phys. Rev. B* **83**, 085426 (2011).
- [43] G. E. Volovik, *The universe in a helium droplet*, Vol. 117 (OUP Oxford, 2003).
- [44] W. Witczak-Krempa, M. Knap, and D. Abanin, Interacting weyl semimetals: Characterization via the topological hamiltonian and its breakdown, *Phys. Rev. Lett.* **113**, 136402 (2014).
- [45] T. Morimoto and N. Nagaosa, Weyl mott insulator, *Scientific Reports* **6**, 19853 (2016).
- [46] L. Crippa, A. Amaricci, N. Wagner, G. Sangiovanni, J. C. Budich, and M. Capone, Nonlocal annihilation of weyl fermions in correlated systems, *Phys. Rev. Res.* **2**, 012023 (2020).
- [47] N. Wagner, L. Crippa, A. Amaricci, P. Hansmann, M. Klett, E. J. König, T. Schäfer, D. D. Sante, J. Cano, A. J. Millis, A. Georges, and G. Sangiovanni, Mott insulators with boundary zeros, *Nature Communications* **14**, 7531 (2023).
- [48] H.-H. Lai, S. E. Grefe, S. Paschen, and Q. Si, Weyl-kondo semimetal in heavy-fermion systems, *Proceedings of the National Academy of Sciences* **115**, 93 (2018).
- [49] L. Chen, F. Xie, S. Sur, H. Hu, S. Paschen, J. Cano, and Q. Si, Emergent flat band and topological kondo semimetal driven by orbital-selective correlations, *Nature Communications* **15**, 5242 (2024).
- [50] S. Bollmann, C. Setty, U. F. P. Seifert, and E. J. König, Topological green's function zeros in an exactly solved

- model and beyond, *Phys. Rev. Lett.* **133**, 136504 (2024).
- [51] I. Garate, Phonon-induced topological transitions and crossovers in dirac materials, *Phys. Rev. Lett.* **110**, 046402 (2013).
- [52] K. Saha and I. Garate, Phonon-induced topological insulation, *Phys. Rev. B* **89**, 205103 (2014).
- [53] B. Monserrat and D. Vanderbilt, Temperature effects in the band structure of topological insulators, *Phys. Rev. Lett.* **117**, 226801 (2016).
- [54] G. Antonius and S. G. Louie, Temperature-induced topological phase transitions: Promoted versus suppressed nontrivial topology, *Phys. Rev. Lett.* **117**, 246401 (2016).
- [55] B. Monserrat and A. Narayan, Unraveling the topology of ZrTe_5 by changing temperature, *Phys. Rev. Res.* **1**, 033181 (2019).
- [56] S. Chen, I. J. Parker, and B. Monserrat, Temperature effects in topological insulators of transition metal dichalcogenide monolayers, *Phys. Rev. B* **109**, 155125 (2024).
- [57] T. c. v. Rauch, H. Nguyen Minh, J. Henk, and I. Mertig, Model for ferromagnetic weyl and nodal line semimetals: Topological invariants, surface states, anomalous and spin hall effect, *Phys. Rev. B* **96**, 235103 (2017).
- [58] A. A. Burkov and L. Balents, Weyl semimetal in a topological insulator multilayer, *Phys. Rev. Lett.* **107**, 127205 (2011).
- [59] See Supplemental Material [url], which includes Refs. ? ? ? ? ? , for a description of the electron and magnon Hamiltonians, and details on the treatment of the electron-magnon interaction.
- [60] G. D. Mahan, *Many-particle physics* (Springer Science & Business Media, 2013).
- [61] Supplementary material, .
- [62] J. A. Hertz and D. M. Edwards, Electron-magnon interactions in itinerant ferromagnetism. i. formal theory, *Journal of Physics F: Metal Physics* **3**, 2174 (1973).
- [63] V. Bonbien and A. Manchon, Symmetrized decomposition of the kubo-bastin formula, *Phys. Rev. B* **102**, 085113 (2020).
- [64] F. Giustino, Electron-phonon interactions from first principles, *Rev. Mod. Phys.* **89**, 015003 (2017).

Supplemental Materials: Electron-Magnon Interaction-Induced Topological Phase Transition in Magnetic Weyl Semimetals

Konstantinos Sourounis* and Aurélien Manchon†
Aix-Marseille Université, CNRS, CINaM, Marseille, France

I. ELECTRONS

The electronic model of a ferromagnetic Weyl Semimetal on a cubic lattice [1], depicted in Fig. 1 (a), with the conventional spin-splitting included is written as

$$H_e = \epsilon_{\mathbf{k}}^0 I_4 + \mathbf{d}_{\mathbf{k}} \cdot \boldsymbol{\sigma} \tau^x + M_{\mathbf{k}} I_2 \tau^z + \Delta \langle S^z \rangle \sigma^z I_2 \quad (1)$$

where $\epsilon_{\mathbf{k}}^0 = 2\gamma(3 - \sum_i \cos k_i)$, $d_{\mathbf{k}} = -2\lambda \sin k_i$, $M_{\mathbf{k}} = m + 2t(3 - \sum_i \cos k_i)$ ($i = x, y, z$). The $\epsilon_{\mathbf{k}}^0$ breaks the particle-hole symmetry, and it can change the interaction-induced topology [1], but this is outside the scope of this work, and we set $\gamma = 0$. The electron Hamiltonian can be written in matrix form

$$H_{\mathbf{k}}^e = \Psi_{\mathbf{k}}^\dagger \begin{pmatrix} \epsilon_{\mathbf{k}}^0 + M_{\mathbf{k}} + \Delta \langle S^z \rangle & 0 & d_z & d_x - id_y \\ 0 & \epsilon_{\mathbf{k}}^0 + M_{\mathbf{k}} - \Delta \langle S^z \rangle & d_x + id_y & -d_z \\ d_z & d_x - id_y & \epsilon_{\mathbf{k}}^0 - M_{\mathbf{k}} + \Delta \langle S^z \rangle & 0 \\ d_x + id_y & -d_z & 0 & \epsilon_{\mathbf{k}}^0 - M_{\mathbf{k}} - \Delta \langle S^z \rangle \end{pmatrix} \Psi_{\mathbf{k}} \quad (2)$$

where the Bloch basis is $\Psi_{\mathbf{k}} = (c_{A,\downarrow}, c_{A,\uparrow}, c_{B,\downarrow}, c_{B,\uparrow})^T$ and is diagonalized by the basis transformation

$$U_{\mathbf{k}}^\dagger H^e(\mathbf{k}) U_{\mathbf{k}} = E_{\mathbf{k}} \quad (3)$$

which let us alternatively write the electron operators as $c_{\eta\uparrow/\downarrow,\mathbf{k}} = \sum_n U_{\eta\uparrow/\downarrow,\nu,\mathbf{k}} \psi_{\nu,\mathbf{k}}$ is the eigenbasis where n is the band index. The spectrum of the electrons, for Fermi level set to zero ($\mu = 0$), is insulating along the k_x, k_y direction, while in the k_z direction it can either be an insulator (I) or form a Weyl semimetal (WSM). We plot the energy spectrum for the cases we study on the paper $m = \pm t$, as well for the intermediate state $m = 0$, along the symmetry path $\Gamma(0, 0, 0) - X(\pi, 0, 0) - M(\pi, \pi, 0) - Y(0, \pi, 0) - Z(0, 0, \pi)$.

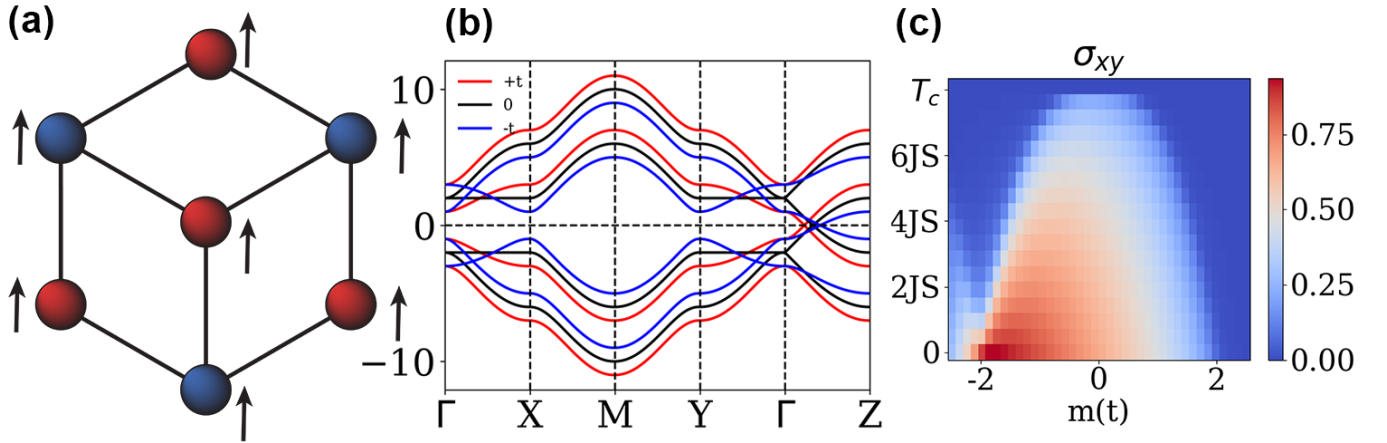


FIG. 1. (a) The ferromagnetic simple cubic lattice with two orbitals. (b) The non-interacting electronic spectrum for $m = \pm t, 0$ along the high-symmetry path. (c) The non-interacting conductivity calculated by Eq. 5 of the material as a function of temperature and mass term.

* konstantinos.sourounis@univ-amu.fr

† aurelien.manchon@univ-amu.fr

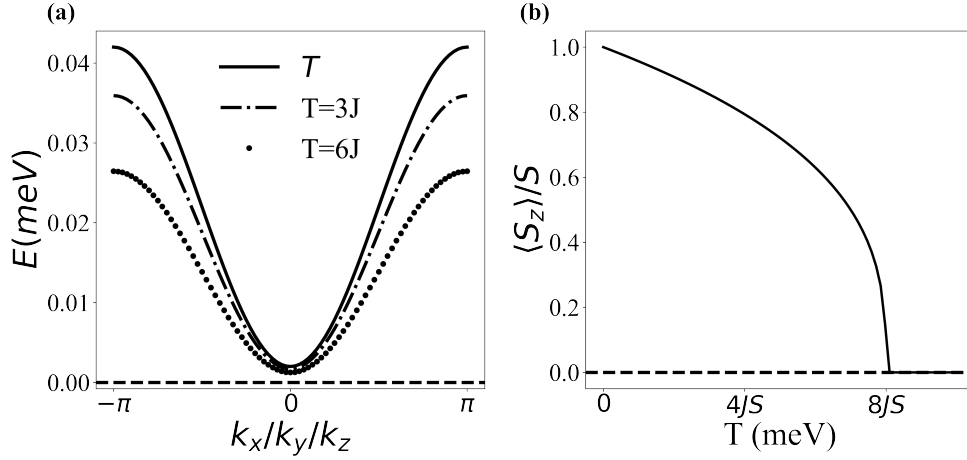


FIG. 2. (a) The magnon spectrum along the k_x, k_y, k_z direction with the renormalized magnetization $\langle S^z \rangle$ (b) The evolution of $\langle S^z \rangle$ under temperature, which is related to the well known Curie magnetization-temperature evolution.

The non-interacting anomalous Hall transport of electrons is described by the following equations

$$\Omega_n^{xy}(k_x, k_y) = 2\text{Im} \sum_{\mu \neq \nu} \frac{(\mathbf{U}_k^\dagger \partial_{k_x} \mathbf{H}_k \mathbf{U}_k)_{\nu\mu} (\mathbf{U}_k^\dagger \partial_{k_y} \mathbf{H}_k \mathbf{U}_k)_{\mu\nu} - (x \leftrightarrow y)}{(\epsilon_{\nu,k} - \epsilon_{\mu,k})^2} \quad (4)$$

$$\sigma_{xy} = \sum_n \int dk_x dk_y dk_z \Omega_n^{xy}(k_x, k_y, k_z) n_F(\epsilon_{\nu,k}) \quad (5)$$

$$C_n(k_z) = \int dk_x dk_y \Omega_n^{xy}(k_x, k_y, k_z) \quad (6)$$

where Ω_n^{xy} describes the Berry curvature of the electrons in the $k_x - k_y$ plane of the n -th band, the integral of the Berry curvature gives the Chern number and σ_{xy} gives the anomalous Hall effect. The anomalous Hall effect in all other directions is zero for the cubic model in the range of parameters we consider. In Fig. 1(c), we plot the transport diagram of the model for various values of m and temperature T , as we consider $S = \langle S^z \rangle$. At $T = 0K$, we can see that the model is on the WSM phase in the range $m = (-\Delta, \Delta)$, and thus has non-zero conductivity. As the temperature increases $T > 0K$, due to the softening of magnetization $\langle S^z \rangle$, the magnitude of the conductivity decreases, until the material becomes an insulator. We note that close to $m=0$, the conductivity goes to zero as the material approaches the Curie temperature ($8JS$) and the material enters the paramagnetic phase. Away from $m=0$, the conductivity goes to zero, and thus the phase transitions from WSM to I, at lower temperatures.

II. MAGNONS

We consider the magnons to be described by the Heisenberg interaction on a cubic lattice

$$H^m = -J \sum_{\langle ij \rangle} \mathbf{S}_i \cdot \mathbf{S}_j + K \sum_i (S^z)^2 \quad (7)$$

By performing the Holstein-Primakoff transformation [2]

$$S_i^+ \approx \sqrt{2S} a_i, \quad S_i^- \approx \sqrt{2S} a_i^\dagger, \quad S_i^z = S - a_i^\dagger a_i, \quad (8)$$

$$(9)$$

and the Fourier transform, $a_k = \frac{1}{\sqrt{N}} \sum_i e^{ikr_i} a_i$, we can write the single band magnon Hamiltonian in momentum space as

$$H^m(\mathbf{k}) = 2JS(3 - \sum_i \cos k_i) + 2KS, \quad (10)$$

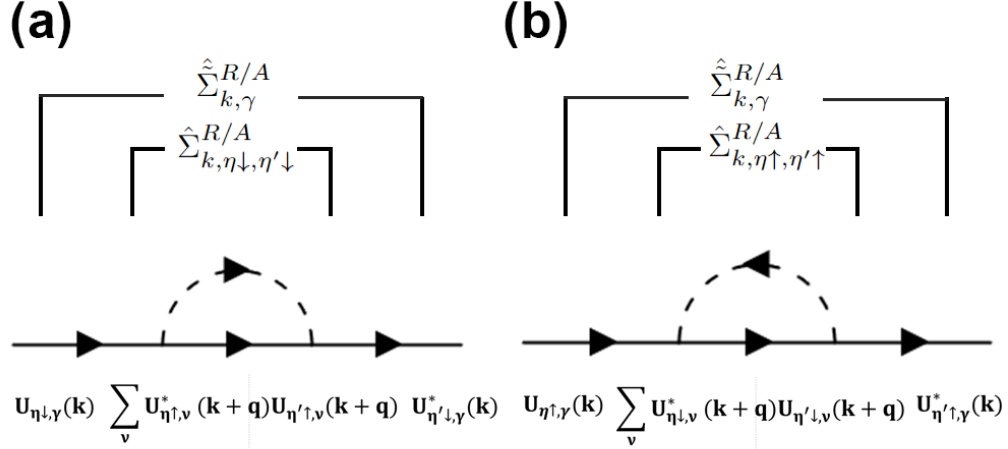


FIG. 3. The Feynman diagrams that describe the self-energy of (a) eq. 20 and (b) eq. 21. The sum of the two diagrams describes eq. 22.

where we have only considered the first term in the Hosten Primakoff transformation, in the approximation of the Linear Spin Wave Theory (LSWT). LSWT is considered accurate in the limit of $k_b T \ll JS$, as the temperature increases to account for the magnetization softening, additional magnon terms must be considered. Instead as discussed in the text, a phenomenological magnetization softening is used, $\langle S^z \rangle = S(1 - T/T_C)^\alpha$, $T_C = 8JS$, $\alpha = 1/3$ for the simple cubic model. The calculation by multiple magnon interactions and $\langle S^z \rangle$ should give qualitatively the same results for this simple magnon model [3]. In Fig. 2, the temperature-dependent magnon spectrum and the magnetization along the temperature are given.

III. MAGNON-ELECTRON INTERACTIONS

A. Self Energies

Here, we will present in detail the theory of the magnon-electron interactions which can account for ferromagnetic multiband materials with spin-orbit coupling. A simpler version of the theory for a one-orbital model was previously derived in [4–6], and an expanded version for a multiband model with spin-orbit coupling was presented in [7]. These works focused on the spectroscopic properties of the interactions. We show how the two theories are connected in the limit of one-band, how band-mixing affects the interactions, and how geometrical properties can be calculated where interactions are accounted for. Finally, we will express the self-energies in both the eigenvalues and the Bloch basis, which is necessary to calculate geometric properties like the Berry curvature. Starting with eq. (3) in the main text

$$\hat{H}^{em} = \Delta (S_i^+ c_{\eta\downarrow,i}^\dagger c_{\eta\uparrow,j} + S_i^- c_{\uparrow\eta,i}^\dagger c_{\eta\downarrow,j} + S_i^z (c_{\eta\uparrow,i}^\dagger c_{\eta\uparrow,j} - c_{\eta\downarrow,i}^\dagger c_{\eta\downarrow,j})) \quad (11)$$

written in real space, where $\eta = A, B$ is the sublattice and by performing the Holstein-Primakoff transformation as described in Section II of the Supplementary Material and the Fourier transform, the electron-magnon interaction can be rewritten as eq. 4 in the main text

$$\begin{aligned} \hat{H}^{em}(\mathbf{k}) = \Delta \sum_{q,\eta} & \left(\sqrt{2S} a_{\mathbf{q}} c_{\eta\downarrow,\mathbf{k}+\mathbf{q}}^\dagger c_{\eta\uparrow,\mathbf{k}} + \sqrt{2S} a_{-\mathbf{q}}^\dagger c_{\uparrow\eta,\mathbf{k}+\mathbf{q}}^\dagger c_{\eta\downarrow,\mathbf{k}} \right. \\ & \left. + (S - a_{\mathbf{q}}^\dagger a_{\mathbf{q}}) (c_{\eta\downarrow,\mathbf{k}}^\dagger c_{\eta\downarrow,\mathbf{k}} - c_{\eta\uparrow,\mathbf{k}}^\dagger c_{\eta\uparrow,\mathbf{k}}) \right) \end{aligned} \quad (12)$$

which is a Hamiltonian nonlinear in operators. The second line is incorporated in the electronic Hamiltonian as the usual spin-splitting, with the additional temperature dependence, we already discussed in Section II. We write the interaction in the diagonalized electrons basis

$$\hat{H}^{em}(\mathbf{k}) = \Delta \sqrt{2S} \sum_{\mathbf{q},\eta,\nu} \left((U_{\eta\downarrow,\nu}^*(\mathbf{k}+\mathbf{q}) U_{\eta\uparrow,\nu}(\mathbf{k})) a_{\mathbf{q}} \psi_{\nu,\mathbf{k}+\mathbf{q}}^\dagger \psi_{\nu,\mathbf{k}} + (U_{\eta\uparrow,\nu}^*(\mathbf{k}+\mathbf{q}) U_{\eta\downarrow,\nu}(\mathbf{k})) a_{-\mathbf{q}}^\dagger \psi_{\nu,\mathbf{k}+\mathbf{q}}^\dagger \psi_{\nu,\mathbf{k}} \right). \quad (13)$$

To calculate its impact, we will follow the well-known method of the phonon-electron problem [8], where we will calculate the self-energies

$$G_{\mathbf{k},\alpha\beta}(\tau) \approx G_{\mathbf{k},\alpha\beta}^{(0)}(\tau) - \frac{1}{2!} \int_0^\beta d\tau_1 d\tau_2 \langle \mathcal{T} \hat{H}^{em}(\tau_1) \hat{H}^{em}(\tau_2) \psi_{\mathbf{k},\alpha}(\tau) \psi_{\mathbf{k},\beta}^\dagger(0) \rangle, \quad (14)$$

where the non-interacting Green's function is $G_{\mathbf{k},\alpha\beta}^{(0)}(\tau) = -\langle \mathcal{T} \psi_{\mathbf{k},\alpha}(\tau) \psi_{\mathbf{k},\beta}^\dagger(0) \rangle$, \mathcal{T} is the time ordering operator and $\beta = 1/k_B T$ and higher orders of interactions are ignored for simplicity. By inserting eq. 13 in eq. 14, applying Wick's theorem and Fourier transform, we get the self-energies of the interactions

$$\Sigma(\mathbf{k}, ip_n) = D^{(0)}(\mathbf{q}, i\omega_n) G^{(0)}(\mathbf{k} + \mathbf{q}, ip_n + i\omega_n). \quad (15)$$

The next step is Matsubara's frequency summation to get the temperature-dependent self-energy correction. We take the self-energy expressions in eq. 15 for the boson-fermion problem and we solve it as follows

$$\Sigma_{\mathbf{k},\eta\downarrow,\eta'\downarrow}(ip_n) = \sum_{\omega_n} \Phi_{\nu,\mathbf{k}+\mathbf{q}}^{\eta\downarrow,\eta'\downarrow} \left(\frac{1}{i\omega_n - \omega_{\mathbf{q}}} \right) \frac{1}{ip_n + i\omega_n - \epsilon_{\nu,\mathbf{k}+\mathbf{q}}}. \quad (16)$$

$$\Sigma_{\mathbf{k},\eta\uparrow,\eta'\uparrow}(ip_n) = \sum_{\omega_n} \Phi_{\nu,\mathbf{k}+\mathbf{q}}^{\eta\uparrow,\eta'\uparrow} \left(-\frac{1}{i\omega_n + \omega_{\mathbf{q}}} \right) \frac{1}{ip_n + i\omega_n - \epsilon_{\nu,\mathbf{k}+\mathbf{q}}}. \quad (17)$$

The above complex analysis problem has two poles for each equation $z_1 = \omega_{\mathbf{q}}$, $z_2 = -\omega_{\mathbf{q}}$ and for both case $z_3 = \epsilon_{\mathbf{k}+\mathbf{q}} - ip_n$ which respectively give the solutions

$$R_1 = \frac{n_B(\omega_{\mathbf{q}})}{ip_n - \epsilon_{\nu,\mathbf{k}+\mathbf{q}} + \omega_{\mathbf{q}}}, \quad R_2 = \frac{n_F(\epsilon_{\nu,\mathbf{k}+\mathbf{q}})}{ip_n - \epsilon_{\nu,\mathbf{k}+\mathbf{q}} + \omega_{\mathbf{q}}} \quad (18)$$

and

$$R_3 = \frac{1 + n_B(\omega_{\mathbf{q}})}{ip_n - \epsilon_{\nu,\mathbf{k}+\mathbf{q}} - \omega_{\mathbf{q}}}, \quad R_4 = \frac{-n_F(\epsilon_{\nu,\mathbf{k}+\mathbf{q}})}{ip_n - \epsilon_{\nu,\mathbf{k}+\mathbf{q}} - \omega_{\mathbf{q}}}. \quad (19)$$

By solving this problem we get the self-energies either in the Bloch basis

$$\hat{\Sigma}_{\mathbf{k},\eta\downarrow,\eta'\downarrow}^{R/A}(\epsilon, T) = \sum_{\mathbf{q},\nu} \Phi_{\nu,\mathbf{k}+\mathbf{q}}^{\eta\downarrow,\eta'\downarrow} \frac{n_F(\epsilon_{\nu,\mathbf{k}+\mathbf{q}}) + n_B(\omega_{\mathbf{q}})}{\epsilon \pm i\Gamma + -\epsilon_{\nu,\mathbf{k}+\mathbf{q}} + \omega_{\mathbf{q}}} \quad (20)$$

$$\hat{\Sigma}_{\mathbf{k},\eta\uparrow,\eta'\uparrow}^{R/A}(\epsilon, T) = \sum_{\mathbf{q},\nu} \Phi_{\nu,\mathbf{k}+\mathbf{q}}^{\eta\uparrow,\eta'\uparrow} \frac{1 - n_F(\epsilon_{\nu,\mathbf{k}+\mathbf{q}}) + n_B(\omega_{\mathbf{q}})}{\epsilon \pm i\Gamma - \epsilon_{\nu,\mathbf{k}+\mathbf{q}} - \omega_{\mathbf{q}}} \quad (21)$$

or their sum gives us the solution in the eigenergies basis

$$\hat{\Sigma}_{\mathbf{k},\gamma}^{R/A}(\epsilon, T) = \sum_{\mathbf{q},\nu} \left(\Phi_{\nu,\mathbf{k}+\mathbf{q}}^{(i)} \frac{n_F(\epsilon_{\nu,\mathbf{k}+\mathbf{q}}) + n_B(\omega_{\mathbf{q}})}{\epsilon \pm i\Gamma + -\epsilon_{\nu,\mathbf{k}+\mathbf{q}} + \omega_{\mathbf{q}}} + \Phi_{\nu,\mathbf{k}+\mathbf{q}}^{(ii)} \frac{1 - n_F(\epsilon_{\nu,\mathbf{k}+\mathbf{q}}) + n_B(\omega_{\mathbf{q}})}{\epsilon \pm i\Gamma - \epsilon_{\nu,\mathbf{k}+\mathbf{q}} - \omega_{\mathbf{q}}} \right) \quad (22)$$

where the summation is over all possible bands weighted by the Φ -matrices,

$$\Phi_{\nu,\mathbf{k}+\mathbf{q}}^{\eta\downarrow,\eta'\downarrow} = \frac{I^2 \langle S^z \rangle}{N} U_{\eta\downarrow,\nu}^*(\mathbf{k} + \mathbf{q}) U_{\eta'\downarrow,\nu}(\mathbf{k} + \mathbf{q}), \quad \Phi_{\nu,\mathbf{k}+\mathbf{q}}^{\eta\uparrow,\eta'\uparrow} = \frac{I^2 \langle S^z \rangle}{N} U_{\eta\uparrow,\nu}^*(\mathbf{k} + \mathbf{q}) U_{\eta'\uparrow,\nu}(\mathbf{k} + \mathbf{q}), \quad (23)$$

and

$$\Phi_{\nu,\mathbf{k}+\mathbf{q}}^{(i)} = \frac{I^2 \langle S^z \rangle}{N} U^*(\mathbf{k}) U^*(\mathbf{k} + \mathbf{q}) U(\mathbf{k} + \mathbf{q}) U(\mathbf{k}), \quad \Phi_{\nu,\mathbf{k}+\mathbf{q}}^{(ii)} = \frac{I^2 \langle S^z \rangle}{N} U_\gamma^*(\mathbf{k}) U^*(\mathbf{k} + \mathbf{q}) U(\mathbf{k} + \mathbf{q}) U_\gamma(\mathbf{k}). \quad (24)$$

In matrix form, the self-energies in the two different basis take the form

$$\hat{\Sigma}_{\mathbf{k}}^{R/A}(\epsilon, T) = \begin{pmatrix} \Sigma_{A\uparrow,A\uparrow}^{R/A} & 0 & \Sigma_{A\uparrow,B\uparrow}^{R/A} & 0 \\ 0 & \Sigma_{A\downarrow,A\downarrow}^{R/A} & 0 & \Sigma_{A\downarrow,B\downarrow}^{R/A} \\ \Sigma_{B\uparrow,A\uparrow}^{R/A} & 0 & \Sigma_{B\uparrow,B\uparrow}^{R/A} & 0 \\ 0 & \Sigma_{B\downarrow,A\downarrow}^{R/A} & 0 & \Sigma_{B\downarrow,B\downarrow}^{R/A} \end{pmatrix} \quad (25)$$

or in the eigenbasis

$$\hat{\Sigma}_{\mathbf{k}}^{R/A}(\epsilon, T) = \begin{pmatrix} \Sigma_1^{R/A} & 0 & 0 & 0 \\ 0 & \Sigma_2^{R/A} & 0 & 0 \\ 0 & 0 & \Sigma_3^{R/A} & 0 \\ 0 & 0 & 0 & \Sigma_4^{R/A} \end{pmatrix}. \quad (26)$$

In Fig. 3, the Feynman diagrams of the magnon-electron interaction are depicted. The process consists of two separate processes. The first (second) is when a magnon is absorbed (emitted) and the spin of the electron changes from down (up) to up (down), and the opposite process completes the many-body interaction. In the presence of spin-orbital coupling and a mixture of the bands, the electron can change the orbital from the initial η to the final η' state. By only taking the intermediate processes (symbolized by $U_{\eta\sigma,\nu}(\mathbf{k} + \mathbf{q})$), we can write the self-energy in the Bloch basis instead of the eigenbasis as done in other works [6, 7] and, as such, we can calculate quantities that depend on the geometry of the wave-functions, such as the Berry curvature and anomalous Hall effect by using Green's function formalism. Throughout this work we will use the Bloch basis, to calculate the Green's functions as

$$G_{\mathbf{k}}^{R/A}(\epsilon) = \frac{1}{(\epsilon \pm i\Gamma - H_{\mathbf{k}}^0 - \hat{\Sigma}_{\mathbf{k}}^{R/A}(\epsilon, T))}. \quad (27)$$

B. Quantum Statistics of the Electron-Magnon Interaction

In a ferromagnetic (semi-)metal, the electrons have a spin polarization, which is symbolized as \uparrow . From a statistical point of view of magnetization, it means that the number of electrons are $N_{\uparrow} \gg N_{\downarrow}$ which corresponds that in average $E_{\uparrow} < E_{\downarrow}$ and electrons prefer to occupy the \uparrow state. This energy difference manifests as an energy splitting between the two states, which is called spin-split and usually is taken as equivalent to 2Δ across the Brillouin zone. As the temperature increases, the magnetization decreases as the spin loses its ordering up to the Curie temperature, where the order is destroyed, and the metal enters the paramagnetic phase. In the second quantization picture, this is depicted by spin-down electrons emitting magnons and flipping to a spin-up state as the temperature increases. Consequently, the spin-split gap must close and thus the magnon interaction should decrease the energy of E_{\downarrow} and increase the energy of E_{\uparrow} , in equivalent values due to the particle-hole symmetry, which corresponds to $\Delta_{eff} = 2\Delta + \Sigma_{\eta,\downarrow} - \Sigma_{\eta,\uparrow}$.

For the $m = +t$ (trivial) regime, the system loses its magnetization process across k_z , with the process increased near the semimetallic region as expected due to electrons near the Fermi level, between the Weyl points. For the $m = -t$ (inverted) regime, the loss of magnetization is slowed around the Γ point due to the reversal of the spin chirality between the Weyl points, which suppresses the spin flips, and thus the magnetization survives in higher temperatures.

C. Numerical Results

We present additional numerical calculations of the self-energies. We plot the real part of the self-energy diagonal elements of eq. 25, which are expected to contribute more than the off-diagonal. In Fig. 4, the dependence of the self-energies on the momentum is plotted for energy set to $\epsilon = 0$. We focus on the $A \downarrow$ and $B \uparrow$ plots, as these points should influence more the Weyl points bands and thus the total topology and transport of the system. We find that at $T = 0K$, the self-energies do not depend on k_z . As the temperature increases for $T > 0K$, the self-energies gain momentum dependence as the thermally excited magnons interact with the electrons. For the two cases, $m = \pm t$, the middle band has an opposite direction between the Weyl points, which illustrates the different impact that the interactions can have, as discussed in the main text.

In Fig. 5, we plot the real part of the self-energies by varying the energy ϵ for $T = 0K$. As the self-energies do not depend on momentum, as explained previously, we choose arbitrarily $k_x, k_y, k_z = 0$, which should generalize to any point on the Brillouin zone. We can see that the central bands are generally smooth under energy variation, and thus, we make the approximation $\partial_{\epsilon/\eta} \Sigma_{\mathbf{k}}(\epsilon, T) \approx 0$.

IV. TOPOLOGY AND TRANSPORT IN INTERACTING SYSTEMS

To calculate the transport and the topology in the interacting limit, it is necessary to employ Green's functions methods due to the dual nature of the interaction. The real part of the self-energy moves and renormalizes the bands

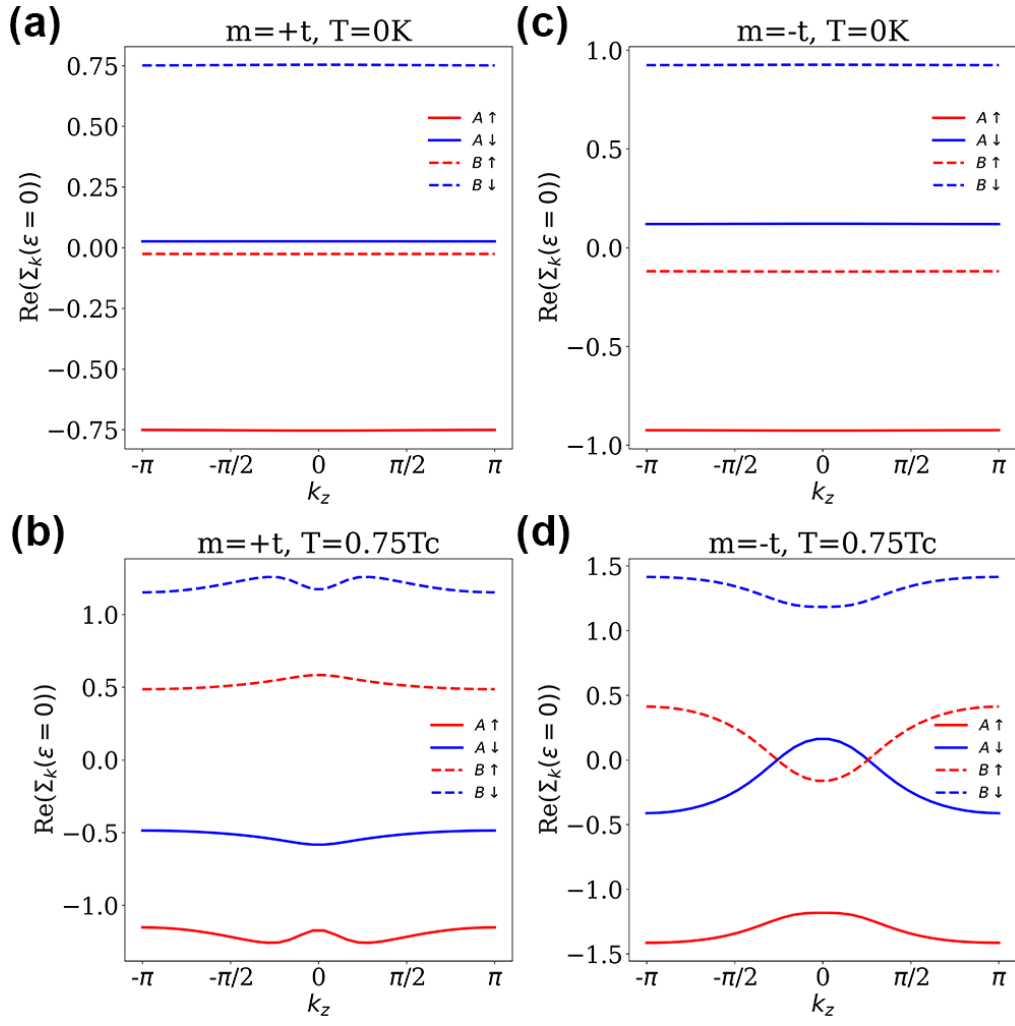


FIG. 4. The calculation of the real part of the diagonal elements of the self-energies $\hat{\Sigma}_k^{R/A}(\epsilon, T)$ for $\epsilon, k_x, k_y = 0$ along the k_z path as the self-energies in eq. 25 for (a) $m = +t, T = 0K$ (b) $m = +t, T = 0.75T_c$ (c) $m = -t, T = 0K$ (d) $m = -t, T = 0.75T_c$.

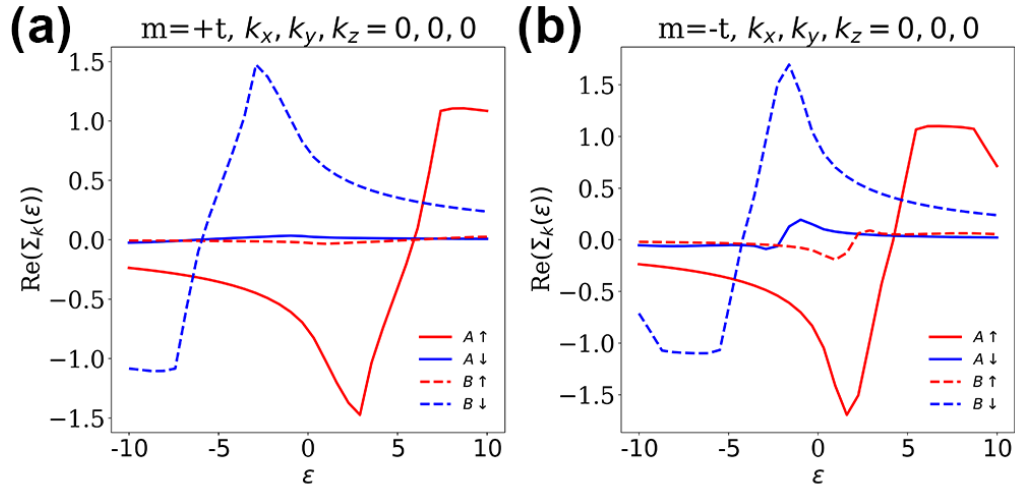


FIG. 5. The calculation of the real part of the diagonal elements of the self-energies $\hat{\Sigma}_k^{R/A}(\epsilon, T)$ for $k_x, k_y, k_z = 0$ and $T = 0K$ by varying the energy ϵ as the self-energies in eq. 25 for (a) $m = +t$ (b) $m = -t$.

(moves the poles), while the imaginary part broadens the well-defined peak of the excitation. We will consider two different types of Green's functions that are similar but have slight differences

$$G_{\mathbf{k}}^T(\eta) = \frac{1}{i\eta - H_{\mathbf{k}} - \Sigma_{\mathbf{k}}(\eta, T)} \quad (28)$$

$$G_{\mathbf{k}}^{R/A} = \frac{1}{\epsilon \pm i\Gamma - H_{\mathbf{k}} - \Sigma_{\mathbf{k}}(\epsilon, T)} \quad (29)$$

the first one is called the topological Green's function while the second are the retarded/advanced Green's functions. The derivatives of the regular and inverse Green's functions are defined as

$$\partial_{\eta}(G_{\mathbf{k}}^T)^{-1} = i - \partial_{\eta}\Sigma_{\mathbf{k}} \quad \partial_{k_i}(G_{\mathbf{k}}^T)^{-1} = -\partial_{k_i}H_{\mathbf{k}} - \partial_{k_i}\Sigma_{\mathbf{k}} \quad (30)$$

$$\partial_{\epsilon}(G_{\mathbf{k}}^{R/A}) = -(G_{\mathbf{k}}^{R/A}) \cdot (1 - \partial_{\epsilon}\Sigma_{\mathbf{k}}) \cdot (G_{\mathbf{k}}^{R/A}) \quad \partial_{k_i}(G_{\mathbf{k}}^{R/A})^{-1} = -\partial_{k_i}H_{\mathbf{k}} - \partial_{k_i}\Sigma_{\mathbf{k}}^{R/A} \quad (31)$$

and $G_{\mathbf{k}}^R = (G_{\mathbf{k}}^A)^{\dagger}$, $\partial_{\epsilon}G_{\mathbf{k}}^R = (\partial_{\epsilon}G_{\mathbf{k}}^A)^{\dagger}$. The two different quantities we calculate based on Green's function are the many-body topological invariant [9]

$$N_3(k_z) = \frac{e^2}{h} \int d\eta \int dk_x dk_y \text{Tr}[G_{\mathbf{k}}^T(\partial_{\eta}G_{\mathbf{k}}^{-1})G_{\mathbf{k}}^T(\partial_{k_x}G_{\mathbf{k}}^{-1})G_{\mathbf{k}}^T(\partial_{k_y}G_{\mathbf{k}}^{-1}) - (x \leftrightarrow y)], \quad (32)$$

which is equivalent to the Berry curvature in momentum space in absence of interactions and then the Fermi sea contribution to the transport [10]

$$\sigma_{xy}(k_z) = \frac{e^2}{h} \int d\epsilon n_F(\epsilon) \int dk_x dk_y \text{Tr}\{\partial_{k_x}G_{\mathbf{k}}^{-1}(G_{\mathbf{k}}^R - G_{\mathbf{k}}^A)\partial_{k_y}G_{\mathbf{k}}^{-1}(\partial_{\epsilon}G_{\mathbf{k}}^R + \partial_{\epsilon}G_{\mathbf{k}}^A) - (x \leftrightarrow y)\} \quad (33)$$

which reduces to the well-know $\sigma_{xy} = \int dk \Omega_n^{xy} n_F(\epsilon_{n,k})$ in the absence of interactions .

-
- [1] I. Garate, Phonon-induced topological transitions and crossovers in dirac materials, *Phys. Rev. Lett.* **110**, 046402 (2013).
[2] T. Holstein and H. Primakoff, Field dependence of the intrinsic domain magnetization of a ferromagnet, *Phys. Rev.* **58**, 1098 (1940).
[3] W. Nolting and A. Ramakanth, *Quantum theory of magnetism* (Springer Science & Business Media, 2009).
[4] R. B. Woolsey and R. M. White, Electron-magnon interaction in ferromagnetic semiconductors, *Phys. Rev. B* **1**, 4474 (1970).
[5] J. A. Hertz and D. M. Edwards, Electron-magnon interactions in itinerant ferromagnetism. i. formal theory, *Journal of Physics F: Metal Physics* **3**, 2174 (1973).
[6] N. H. Jo, Y. Wu, T. V. Trevisan, L.-L. Wang, K. Lee, B. Kuthanazhi, B. Schrunck, S. L. Bud'ko, P. C. Canfield, P. P. Orth, and A. Kaminski, Visualizing band selective enhancement of quasiparticle lifetime in a metallic ferromagnet, *Nature Communications* **12**, 7169 (2021).
[7] K. Mæland, H. I. Røst, J. W. Wells, and A. Sudbø, Electron-magnon coupling and quasiparticle lifetimes on the surface of a topological insulator, *Phys. Rev. B* **104**, 125125 (2021).
[8] G. D. Mahan, *Many-particle physics* (Springer Science & Business Media, 2013).
[9] W. Witczak-Krempa and Y. B. Kim, Topological and magnetic phases of interacting electrons in the pyrochlore iridates, *Phys. Rev. B* **85**, 045124 (2012).
[10] V. Bonbien and A. Manchon, Symmetrized decomposition of the kubo-bastin formula, *Phys. Rev. B* **102**, 085113 (2020).